Materials & Design 222 (2022) 111037

Contents lists available at ScienceDirect

Materials & Design

journal homepage: www.elsevier.com/locate/matdes

Torsion of a rectangular bar: Complex phase distribution in 304L steel revealed by neutron tomography

Khanh Van Tran [a,b,c,*], Robin Woracek [d], Nikolay Kardjilov [a,*], Henning Markötter [a,g], Daniel Abou-Ras [a], Stephen Puplampu [e], Christiane Förster [a], Dayakar Penumadu [e], Carl F.O. Dahlberg [f], John Banhart [a,b], Ingo Manke [a,b]

[a] Helmholtz-Zentrum Berlin für Materialien und Energie GmbH, Hahn-Meitner-Platz 1, 14109 Berlin, Germany
[b] Technische Universität Berlin, Straße des 17. Juni 135, 10623 Berlin, Germany
[c] Thuyloi University, 175 Tay Son, Dong Da, Hanoi, Vietnam
[d] European Spallation Source ESS ERIC, SE-221 00 Lund, Sweden
[e] The University of Tennessee, Knoxville, TN 37996-2313, USA
[f] Department of Engineering Mechanics, Royal Institute of Technology, Teknikringen 8D, 10044 Stockholm, Sweden
[g] Bundesanstalt für Materialforschung und -Prüfung, Unter den Eichen 87, 12205 Berlin, Germany

HIGHLIGHTS

- Neutron imaging reveals phase transformation behavior of metastable austenitic stainless steels under plastic deformation.
- 3D mapping of phase distributions in polycrystalline materials non-destructively.
- In-situ investigation of the effect of a geometrical factor on phase transformation in a rectangular TRIP steel sample under torsion load.
- New non-destructive spectroscopic technique based on neutron diffraction contrast is eligible for study of material phase.

GRAPHICAL ABSTRACT

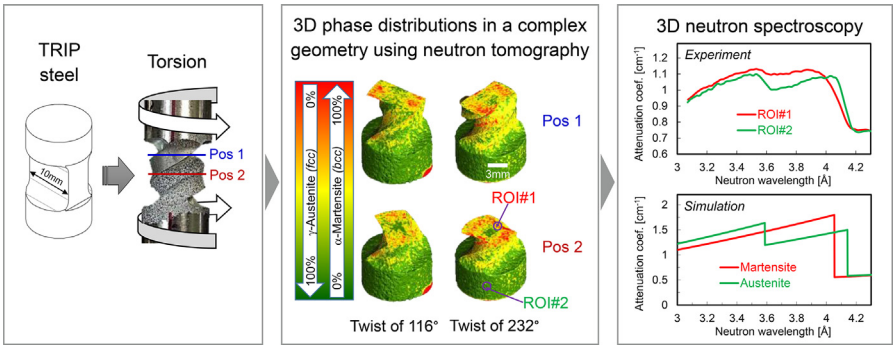

ARTICLE INFO

Article history:
Received 27 April 2022
Revised 28 July 2022
Accepted 5 August 2022
Available online 8 August 2022

Keywords:
Neutron tomography
Phase distribution
Rectangular cross-section
Torsion
Geometrical effect

ABSTRACT

Metastable austenitic stainless steel (304L) samples with a rectangular cross-section were plastically deformed in torsion during which they experienced multiaxial stresses that led to a complex martensitic phase distribution owing to the transformation induced plasticity effect. A three-dimensional characterization of the phase distributions in these cm-sized samples was carried out by wavelength-selective neutron tomography. It was found that quantitatively correct results are obtained as long as the samples do not exhibit any considerable preferential grain orientation. Optical microscopy, electron backscatter diffraction, and finite element modeling were used to verify and explain the results obtained by neutron tomography. Altogether, neutron tomography was shown to extend the range of microstructure characterization methods towards the meso- and macroscale.

* Corresponding authors at: Helmholtz-Zentrum Berlin für Materialien und Energie GmbH, Hahn-Meitner-Platz 1, 14109 Berlin, Germany (K.V.T.).
E-mail addresses: khanhtv@tlu.edu.vn (K.V. Tran), kardjilov@helmholtz-berlin.de (N. Kardjilov).

https://doi.org/10.1016/j.matdes.2022.111037
0264-1275/

1. Introduction

Continued alloy development of steels enables yet improved properties, which result from a carefully balanced microstructure. The tools for microstructure characterization are the backbone to facilitate this progress and are often used in the development of phenomenological or empirical models. Current challenges are often related to the complexity of deformation mechanisms and particularly their interactions across different length scales [1]. While the modeling community has developed sophisticated micromechanical full-field crystal modeling tools that include important microstructure properties [2–10], the available experimental capabilities are lacking the ability to capture microstructure variations on a macroscale. Neutron experiments have long played a vital role in characterizing microstructural properties within the bulk of larger samples [11,12]. More recently, neutron imaging techniques that exploit scattering and diffraction [13–15] have shown the potential to bridge the gap between various length scales.

In the present case study, we visualized spatially varying martensitic phase transformations in three dimensions (3D) that occurred owing to the transformation-induced plasticity (TRIP) effect in metastable stainless steel. The particularity of this study is the rectangular cross-section of the investigated samples that were plastically deformed in torsion, which resulted in complex strain and stress states with spatial variations within the sample. The need and benefit of materials characterization in 3D have been long recognized, as it "provides new insights into how phase distribution, crystallographic interfaces, and defect arrangements contribute to building a material structure" [16]. Commonly applied 3D characterization routines include automated serial sectioning, focused ion beam/scanning electron microscopy (FIB/SEM), X-ray microtomography (microCT), and 3D X-ray diffraction based on laboratory and synchrotron X-ray sources. Neutron tomography is increasingly being used in materials research since it allows for probing deeply into many materials while being sensitive to many light elements [14]. Fig. 1 outlines different 3D characterization techniques in terms of volume and voxel dimensions (note that voxel is used for 3D representation like the pixel is used for 2D representation).

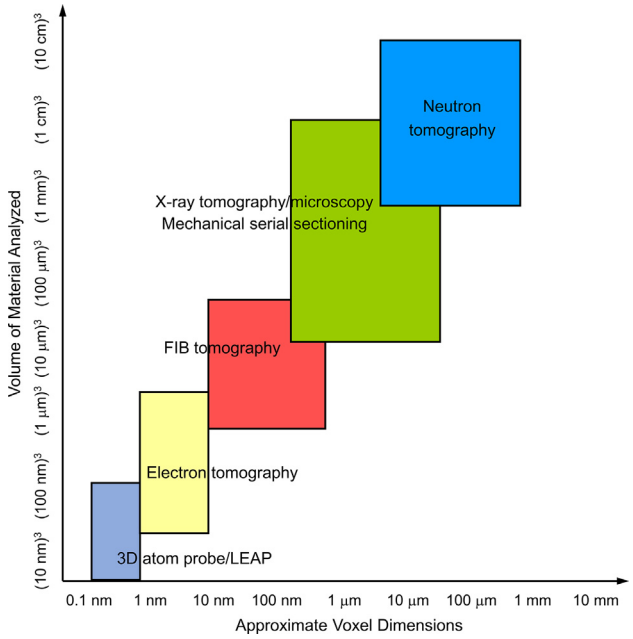

Fig. 1. Overview of available 3D tomographic methods as well as their spatial resolutions and typically analyzed volumes. Neutron tomography enables a non-destructive evaluation of the microstructure across the meso- and macroscale. (Adapted from Ref. [17]).

We previously established that diffraction contrast in neutron imaging could be used for 3D tomographic reconstructions of localized phase fractions within cm-sized TRIP steel samples that were plastically deformed in tension and torsion [18]. The circular sample geometry that was utilized in these studies, however, presented a rather simple case compared to the present study. Another important consideration for diffraction contrast imaging to yield useful results relates to the directional dependence of the diffraction phenomenon: The diffracted neutron intensities are a function of the grain orientation, and hence the same applies for the transmitted intensity. If too many grains within the specimen possess preferred orientations (texture), then the recorded intensity becomes a function of the physical sample orientation (note that this holds true for transmission images as well as diffractograms). Only if the grains are randomly distributed, non-tensorial properties such as crystalline phase fractions can be reconstructed from transmission images alone [18–22]. For samples with preferred grain orientations (texture), however, the widely utilized filtered back-projection algorithm is not applicable, even for the reconstruction of non-tensorial properties. It should also be noted that 2D investigations (radiography) or diffraction with limited angular coverage are obviously prone to the same "(-texture) bias" [23]. The reconstruction of tensorial properties can almost be deemed a research topic in itself [24,25].

While some studies of phase transformations under torsional loading of circular specimens using neutron imaging and X-rays have been reported [18,26], studies of complex geometries under torsional loading are very limited [27,28]. A recent case study reported on spatially resolved phase transformation by 2D neutron radiography in cruciform samples under load path changes [29]. Non-circular and in particular rectangular profiles are very important in engineering practice as they often experience shear stress due to torsion. Analytical solutions for non-circular members under torsion are rarely found as they can be complex and are specific to special shapes of bodies and loads. Hence, numerical tools such as the finite-element, the finite-volume, or the boundary-element method are most commonly applied in cases where the geometry of the sample deviates from the simplest cases. Additionally, they can be coupled with material point models, e.g., models that describe how a material deforms under applied load. For instance, powerful and sophisticated modeling efforts have been and are being undertaken. Comprehensive crystal plasticity computational frameworks are, for example, provided by the Düsseldorf Advanced Material Simulation Kit (DAMASK) [30], CPFEM [31], MOOSE [32], PRISMS-Plasticity [33] or WARP-3D [34]. The combination of in-situ diffraction and crystal plasticity finite element modeling can be used to e.g. analyze the lattice strain evolution in different crystallographic phases [35–38].

In the present case study, we employed optical microscopy and electron backscatter diffraction (EBSD) to verify the results that were obtained by neutron tomography. The corresponding results combined with Finite Element Modelling (FEM) help to interpret the complex spatially varying distribution of the newly formed martensitic phase.

2. Material and methods

2.1. Material and geometry of samples

A well-characterized metastable stainless steel (ASTM standard 304L) was chosen, in which the martensitic phase transformation can be induced by straining the sample at room temperature due

to the TRIP effect. The TRIP effect helps to increase ductility while maintaining high strength as the harder martensite phases (consisting of bcc and hcp structures [39]) act as barriers to dislocation motion during straining. This results in increased strain hardening of the parent fcc austenite [40,41]. It is this phenomenon that prevents early material failure since the transformation occurs more readily at locations where the strain concentration is highest.

The composition of the utilized steel is given in Table 1. Bulk texture analysis was performed previously on exactly the same batch of raw material that was used to manufacture the samples used herein, showing a very mild to nearly random texture [42].

From the as-received material, three samples for torsion experiments were machined to the dimensions shown in Fig. 2. The reason for using the relatively short gauge length was to maximize the achievable shear strains. The samples were deformed to different angular twists of 116°, 232°, and 464°.

2.2. Mechanical deformation and digital image correlation

All three samples were plastically deformed by twisting to the above-mentioned target angles using a deformation rate $\dot{\theta}$ of 10° per minute (0.0029 rad·s^{-1}) at 'room temperature', i.e. ~20 °C. A custom-built load frame [42,43] was used for mechanical deformation. The sample was held under a constant axial seating load of 20 MPa during the torsional deformation. The torque vs twist and shear stress vs twist can be seen in Fig. S2 of the Supplementary Information (SI).

During mechanical deformation, surface strains were measured by digital image correlation (DIC) using the commercial software VIC-3D [44]. Fig. 3 shows the spatial distribution of shear strain (γ_{xy}) on the surface of one of the long sides for a few distinct levels of twisting (note that the surface strain could not be calculated anymore beyond 121°). For instance, at all monitored twist states, the strain magnitude (γ_{xy}) is the largest at the center of the surface as expected, while the locations close to the end (edge) of the sample show values close to zero. At a twist of 9.3°, the center of the sample shows a value of $\gamma_{xy} \approx -0.0156$ and at 84.1°, a value of $\gamma_{xy} \approx -0.8$. It can also be seen from the surface strain maps how the length of the gauge section has important implications for the 'idealized' strain distribution, i.e., the horizontally varying strain distribution is homogenous only within a ~2.5 mm vertical section along the gauge length (height).

The maximum shear stress vs shear strain curve obtained for the center of the surface (indicated as ROI#1) can be seen in Fig. S3 of the SI.

2.3. Neutron wavelength-selective radiography and monochromatic tomography

One of the most relevant contrast mechanisms in neutron imaging of crystalline materials is based on a diffraction phenomenon [16], and hence a short summary shall be given here. Bragg scattering from atomic lattice planes that have distances of d_{hkl} is commonly utilized to study the structure of crystalline materials. A diffracted signal is detected against a weak background, and diffractograms can be recorded wavelength and/or angular dispersive. In cases where the incident radiation is able to penetrate through the sample so that transmission measurements can be performed, the diffracted (coherently scattered) signal is removed from the incident beam intensity, i.e., the beam is attenuated. Neutron (transmission) imaging typically employs neutron wavelengths ranging from ~2 Å to ~6 Å. Considering the structure of the most commonly utilized crystalline materials, this range includes wavelengths at which Bragg scattering does not occur anymore from certain lattice plane families because it is larger than $2d_{hkl}$, the so-called Bragg cut-off. For single crystals, one observes characteristic dips in the wavelength-resolved transmission spectrum (the position depending on the sample orientation), while for randomly orientated polycrystalline materials, a 'saw-tooth' pattern is observed with a sharp increase in transmitted intensity every time the wavelength exceeds the Bragg cut-off for a certain lattice plane family. The positions of these so-called Bragg edges therefore provide a direct measure of d_{hkl} (occurring at $2d_{hkl}$) and carry information about the crystalline structure, including the

Table 1
Chemical composition (wt.%) of the 304L stainless steel used.

C	Co	Cr	Cu	Mn	Si	Mo	N	Ni	P	S	Fe
0.022	0.03	18.18	0.14	1.54	0.29	0.11	0.076	8.55	0.026	0.0017	Balance

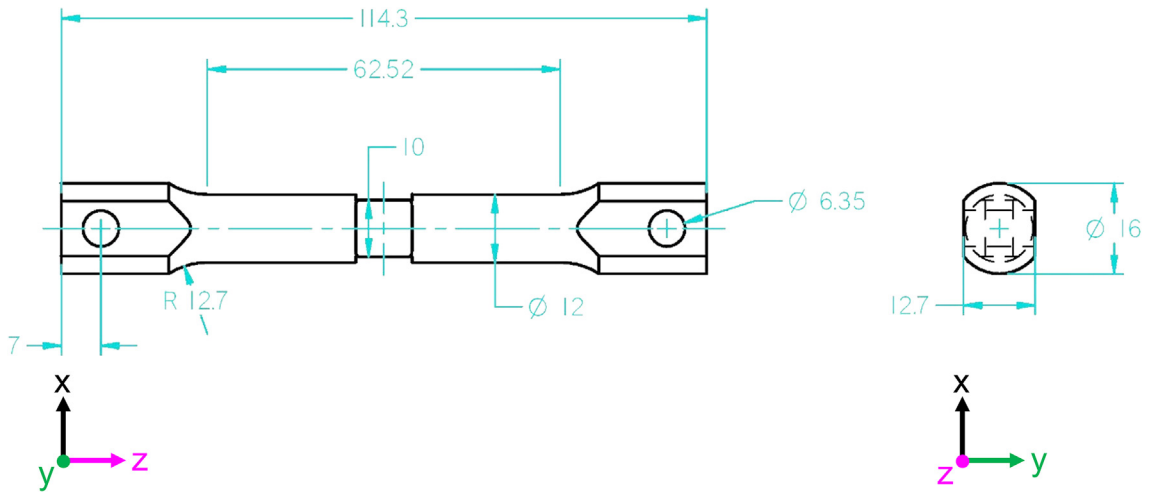

Fig. 2. The geometry of the specimen with dimensions in mm, where the gauge section is 10 mm × 5 mm.

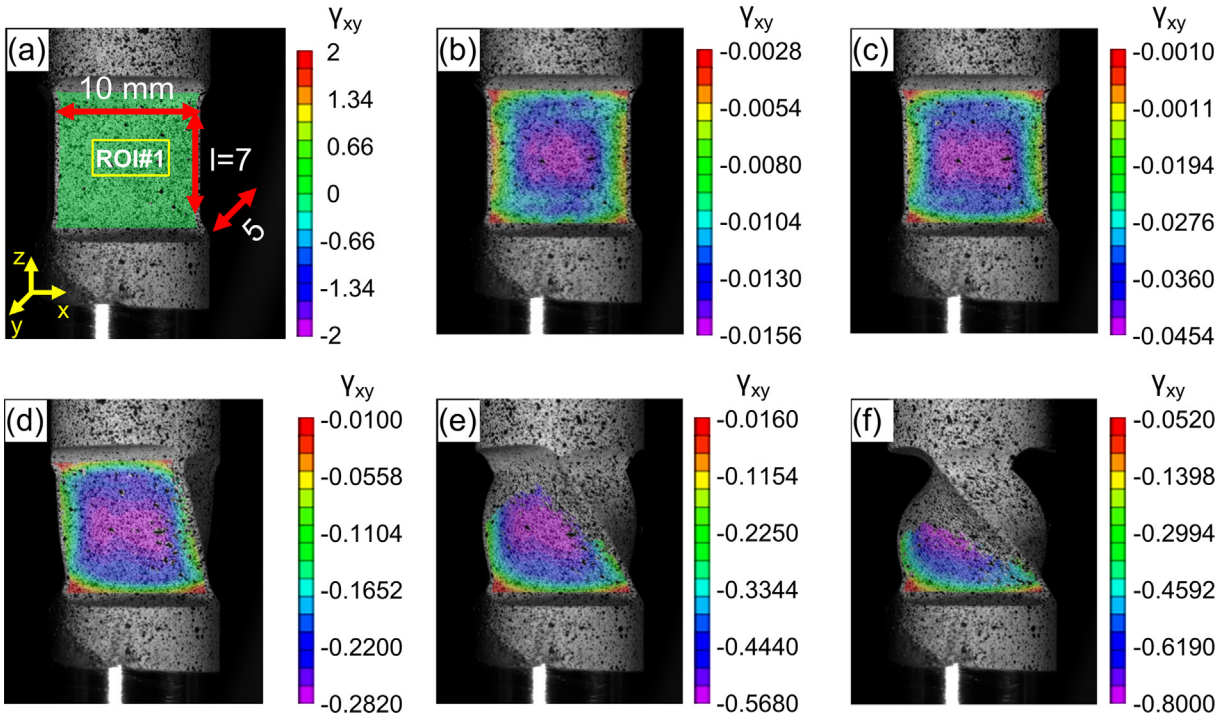

Fig. 3. DIC images of the 304L stainless steel sample twisted stepwise to an angle of 84.1°. (a) Sample surface before the test, (b) twist angle of 9.3°, (c) 12.1°, (d) 39.6°, (e) 64.4° and (f) final twist angle of 84.1°.

type of phase, lattice strain, and preferred grain orientations (texture). In order to utilize diffraction contrast in an imaging experiment, wavelength-resolved measurements are needed that can be realized most commonly by using a tuneable neutron monochromator or by wavelength-dispersive time-of-flight measurements [13,23,45–49].

For the work presented herein, the CONRAD-II imaging instrument [50] at the research reactor BER-II with its tunable monochromator was used. As the first experimental characterization step, a neutron wavelength scan was performed for all the samples in one radiographic projection. The data shown herein was recorded for a wavelength band between 3.0 Å and 4.3 Å by incrementally changing the double crystal monochromator in steps of 0.02 Å and recording images with an exposure time of 120 s at each wavelength. In order to facilitate comparisons of the spectra for different sample regions, the results are normalized to the value after the Bragg cut-off (where no more Bragg diffraction occurs) and also expressed as attenuation coefficient following expression $\Sigma = -\ln(T(\lambda))/d$, where Σ is the attenuation coefficient, d the sample thickness and $T(\lambda)$ is the wavelength-dependent transmission. The sample thickness for the location at the given projection was established from neutron tomography. The measurement time for the transmission spectra presented in Fig. 5 was ~13 h (with 6.5 h each for the sample and 'empty beam' measurement). This relatively long exposure time for one projection is the main reason that we did not perform spectral tomography as recently presented [20,23,51] but used only a few distinct wavelengths for the tomographic reconstructions.

2.4. Optical microscopy and EBSD

For optical microscopy, a Zeiss Axiophot 2, and for EBSD, a Zeiss UltraPlus scanning electron microscope equipped with an Oxford Instruments NordlysNano camera and the AZtec acquisition software were used. The sample deformed to 232° was cut in the middle, where it had undergone the biggest strain. Then the sample was ground by using grinding papers in a sequence from coarse to fine grade. The next step involved a thorough diamond polish on a medium soft cloth and the final polish with colloidal silica to remove the fine scratches. Finally, the sample was etched by a solution of 100 ml water, 100 ml hydrochloric acid, 10 ml nitric acid at a temperature of 50 °C in 5 min for microstructural examination by optical microscopy and EBSD.

2.5. Finite element modeling

In order to interpret the 3D phase distribution that was found by neutron tomography, non-linear finite element modeling was carried out using the software package ABAQUS.

The geometry of the torsion specimen and the three-dimensional finite element mesh used for the simulations are shown in Fig. 2 and Fig. 4a, respectively. Eight-node linear brick elements with reduced integration and hourglass control (C3D8R in ABAQUS Explicit) were used in the gauge section. Since quadrilateral elements cannot be used to produce a structured mesh in non-prismatic regions, four-node linear tetrahedron elements (C3D4 in ABAQUS Explicit) were used outside the central region. This compromises the mesh quality somewhat, but it is deemed a minor issue since the circular cross-section regions remain almost entirely elastic. The element side length was 500 μm for the whole model, and the mesh is shown in Fig. 4a.

For this study, we only have strain data measured by DIC for a twist angle of 135° in torsion and experimental uniaxial tensile strain data up to 0.204. In order to simulate the sample deformed to 232°, one can combine the use of hardening laws to be able to fully simulate the behavior to the desired twist. In this study, a power-law hardening Eq. (1).

$$\sigma_y = \sigma_0 + k\left(\frac{\varepsilon_p}{\varepsilon_0}\right)^m, \tag{1}$$

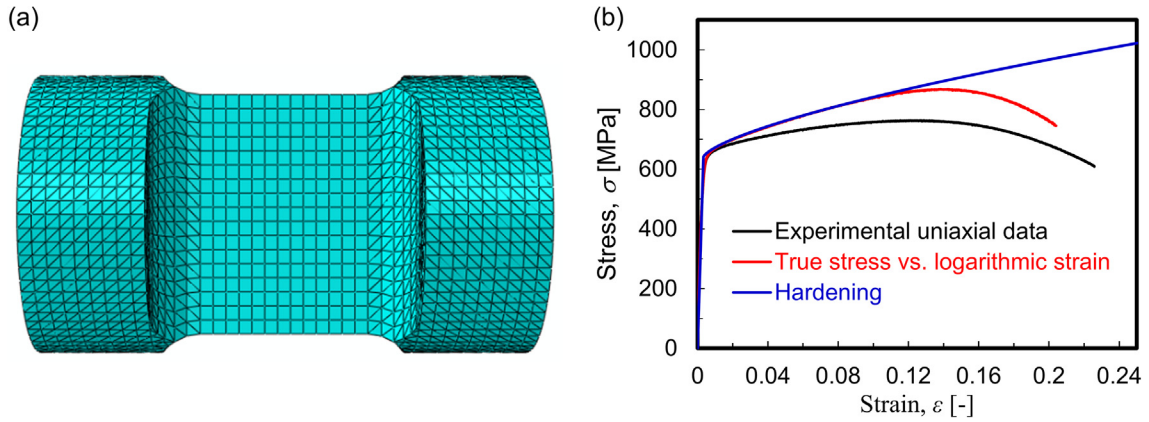

Fig. 4. The finite element mesh and data were used in the finite element analysis. (a) Sample model with the finite element mesh, where the gauge section is 10 mm × 5 mm. (b) Experimental uniaxial data and hardening curves were used for the simulation.

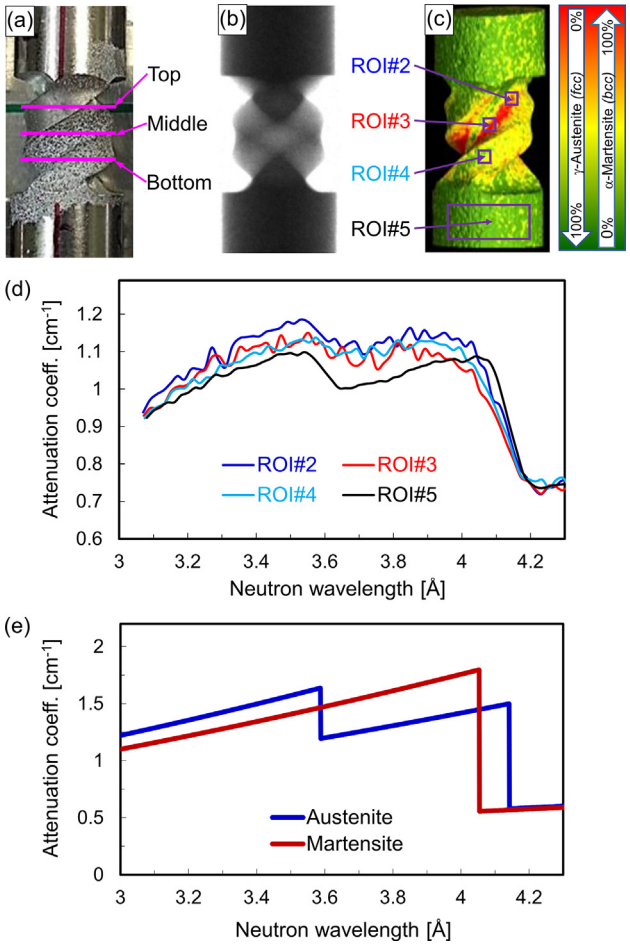

Fig. 5. Images and attenuation coefficient spectra for the sample twisted to 232°: (a) Photo of the sample, (b) Neutron radiographic image of the sample, (c) Neutron tomographic visualization of the sample with regions of interest (ROI) depicted, (d) Attenuation coefficient spectra for the ROIs depicted in (c), (e) Theoretical attenuation coefficient spectra.

was used where $\sigma_0 = 640$ MPa, $k = 20$ MPa, $m = 0.684$ and $\varepsilon_0 = \sigma_0/E = 0.0033$. The parameters in the hardening law were extracted from the true uniaxial stress vs logarithmic strain by a least square regression fit to the data up to 11 % strain (before necking). For strains beyond this point, the model is an extrapolation, as shown in Fig. 4b. However, as the deformation mode is dominated by shearing, the same type of uniaxial necking behavior is not expected, and the extrapolation to strains beyond this can be somewhat motivated. To enable a direct comparison with the experimental results, the model was loaded in the same steps as in the neutron experiments to understand clearly the behavior of the sample. For this purpose, one end of the sample was fixed while the other end was twisted up to 232°.

3. Results and discussion

3.1. Neutron wavelength-selective imaging for phase transformation

The interpretation of transmission spectra through 3D objects of irregular shape is obviously a non-trivial task as they contain information integrated along the beam path through the sample. Nonetheless, evidence is provided that a localized phase transformation from austenite to martensite has occurred: ROI#5 in Fig. 5 corresponds to the undeformed and hence almost pure austenitic phase (assumed for simplicity, while in reality, a small volume fraction of martensite is present as well) and exhibits two distinct Bragg edges, namely fcc(111) at ~4.14 Å and fcc(200) at ~3.59 Å. On the other hand, martensite possesses only one Bragg edge within this wavelength range, namely the one corresponding to bcc(110) at ~4.05 Å. As the Bragg edges corresponding to fcc (111) and bcc(110) are in close proximity, the wavelength resolution of the instrument is not sufficient to observe distinct edges. Regions that have undergone a more pronounced martensitic phase transformation actually show what we observe as a broadening of the Bragg edge around 4 Å that is accompanied by a decreased amplitude of the fcc (200) Bragg edge.

For the same batch of material (same rod), we have shown previously [18] that the as-received material does not exhibit strong texture, more particularly that the wavelength-dependent transmission spectrum does not change notably as a function of sample orientation. This is an important pre-requisite for neutron diffraction contrast imaging to yield meaningful results and to be extended to tomography. While it is unclear if the new phase forms with a preferred crystallographic orientation under torsional loading of the rectangular cross-section, we have previously shown that macroscopic texture evolution is only weak for this specific batch of material when deformed in tension and torsion of a circular cross-section [42].

Tomography at three distinct wavelengths was performed for all three pre-deformed samples by acquiring 180 projections over an angular range of 360°. The exposure time for each projection was 225 sec (three images of 75 sec) and the same for the three

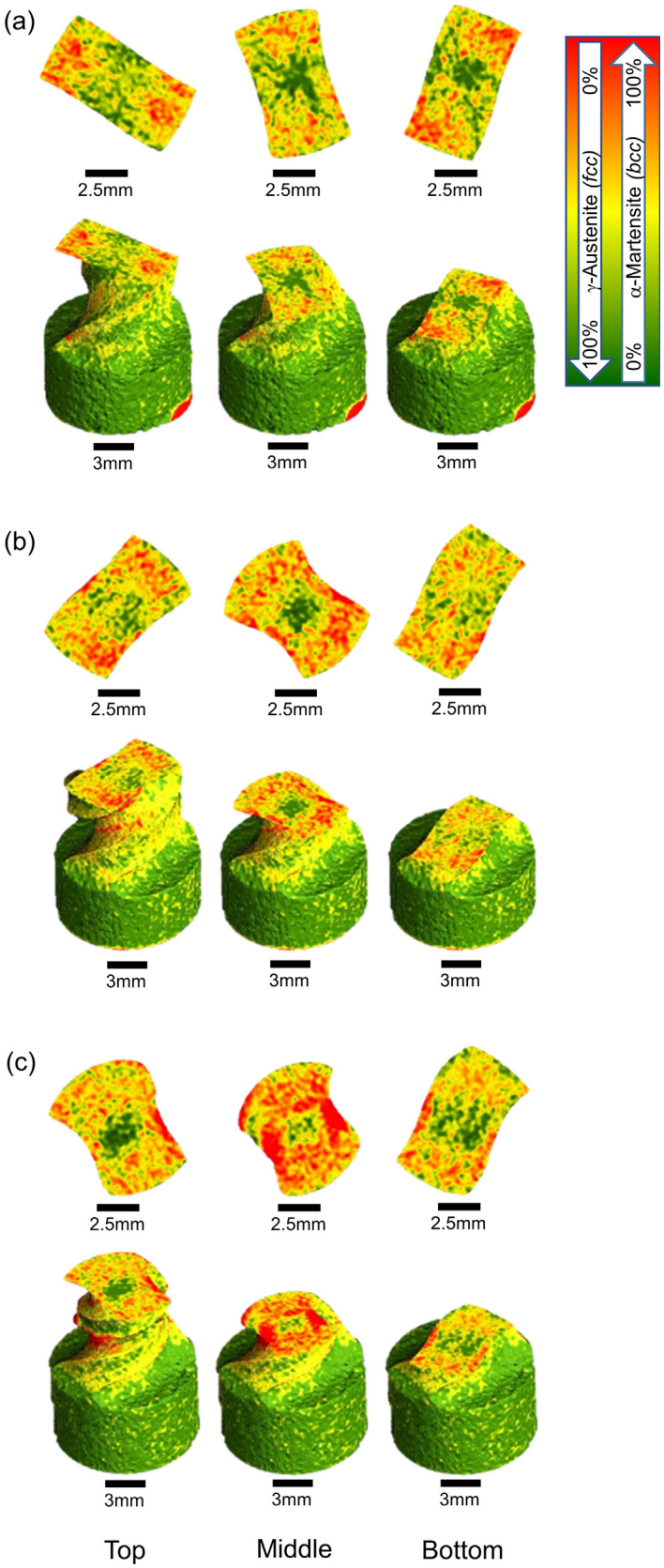

Fig. 6. 3D reconstruction for a neutron wavelength of 3.8 Å where the attenuation coefficient readily indicates the phase distribution. The samples were digitally cut at three positions of the gauge region as defined in Fig. 5a. (a) Twist angles 116°, (b) 232°, (c) 464°.

neutron wavelengths of 3.80 Å, 4.04 Å, and 4.20 Å. Each tomography therefore took ~11.25 h. Tomographic reconstructions of data obtained at 3.80 Å are shown in Fig. 6, where the attenuation coefficient increases from green to red color. At this wavelength, the attenuation coefficient of martensite is larger than that of austenite (see Fig. 5e), and hence the visualization depicts the relative distributions of the two phases. A larger twist angle results in larger amounts of martensite, and furthermore, it can be seen that certain regions within the gauge section show more martensite than others and that the region outside the gauge section does not show signs of phase transformation as expected.

As one expects the phase transformation to occur in regions that experience the highest degree of deformation, the results may appear a little surprising at first when considering the stress distribution in rectangular bars under torsional deformation according to the theory of elasticity, which predicts the highest magnitude of strain in the middle of the long side and zero strain in the four corners [52]. However, the applied deformation takes the specimen well beyond the elastic range and the geometrical boundary conditions differ from these considerations; hence the results are less surprising considering these aspects. Nonetheless, the transformation behavior can indeed be linked to regions that start to experience stress concentrations already at low deformation levels, as will become evident from the discussion presented together with the FEM results. A determining factor is indeed the utilized gauge length, as we will show, and from the neutron tomography results, one can readily observe that there are significant variations of phase distributions within the cross-section at different heights of the gauge length. Three 'cuts' at different heights are presented in Fig. 6. The previously illustrated DIC results have also shown that the surface strain profile varies along the gauge length, with the highest surface shear strains occurring at the center of the gauge length.

3.2. Microstructural characterization

After the non-destructive neutron tomography, the sample that was deformed to 232° was sectioned for further microstructural examination by optical microscopy and EBSD. Optical micrographs of the middle of the cross-section are shown in Fig. 7. A spatially dependent martensitic phase transformation is seen in these images, where the center of the sample exhibits a typical austenitic grain structure with visible slip bands inside the grains. The amount of slip bands increases when moving away from the center

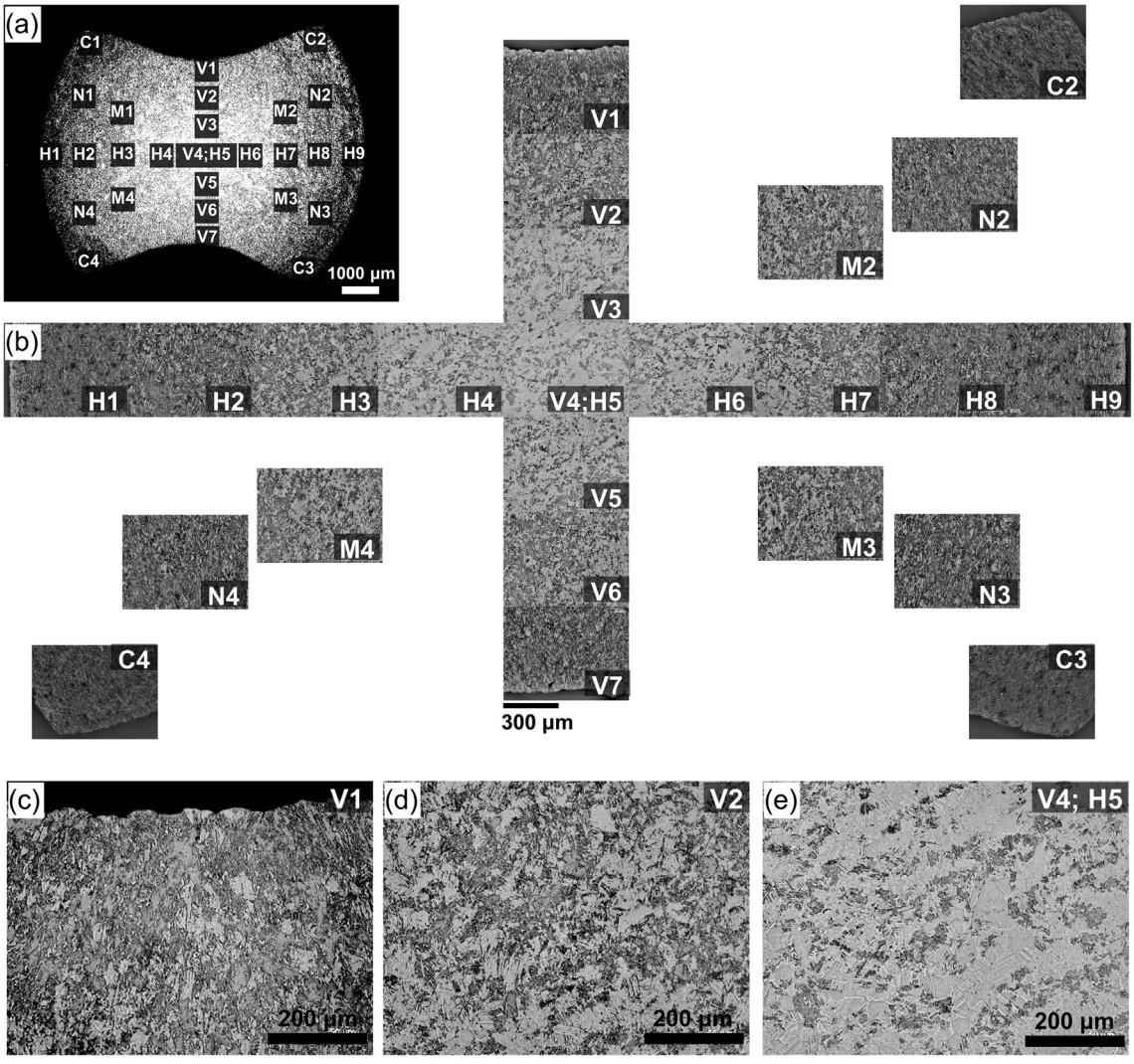

Fig. 7. Optical micrographs were obtained for the cross-section in the middle of the gauge length for the sample twisted to 232°. (a) Low-magnification overview indicating locations of higher-magnification images. (b) Individual micrographs show that the phase transformation increases away from the center of the sample. (c–e) Higher-magnification images from the center towards the long side of the cross-section.

and, at the same time, the micrographs indicate a higher amount of plastic deformation and the formation of martensite. This formation is most pronounced towards the long and short sides of the cross-section. It can be concluded that neutron tomography at 3.8 Å (compare Fig. 6b middle) and optical microscopy correlate very well.

The same cross-section was further investigated using EBSD, with results shown in Fig. 8. The center region (indicated as ROI#6) shows an area fraction of 77 % austenite, 8 % martensite, and 15 % of 'zero solution', i.e., where no successful indexing of the EBSD patterns was possible. The 'zero solution' fraction increases in regions outside the center where higher amounts of plastic deformation have taken place, resulting in faint Kikuchi patterns that were difficult to index [53–58]. The other regions exhibit markedly less austenite, varying between 22 % for ROI#8 (center of long side), 15 % for ROI#7 (center of short side), and 12 % for ROI#9 (corner of the sample). A reliable quantification was not feasible due to poor indexing. Making the reasonable assumption that the the 'non-identified' regions have the same austenite to martensite ratio, or are even fully transformed to martensite, there is a clear qualitative agreement between EBSD, optical microscopy, and neutron wavelength-selective tomography.

3.3. Simulation results of torsion deformation

For the simulations, only a single phase was considered and the TRIP effect was not taken into account. This could be done in the future and by, for example, implementing material point models and a homogenization scheme using programs like DAMASK similar to the work presented in reference [59]. For the present case study, the interpretation of shear strain variations and the relation to the martensitic phase transformation is considered reasonable, yet knowing that the progressing phase transformation and associated stiffness differences likely influence the further development of the transformation kinetics.

The results of the FEM simulation are presented in Fig. 9, where the von Mises stress is shown. As expected, its magnitude increases appreciably with increased twist angles (Fig. 9a–f). The simulation also captures that the von Mises stress is smaller towards the top and bottom of the gauge section. The magnitude is much reduced

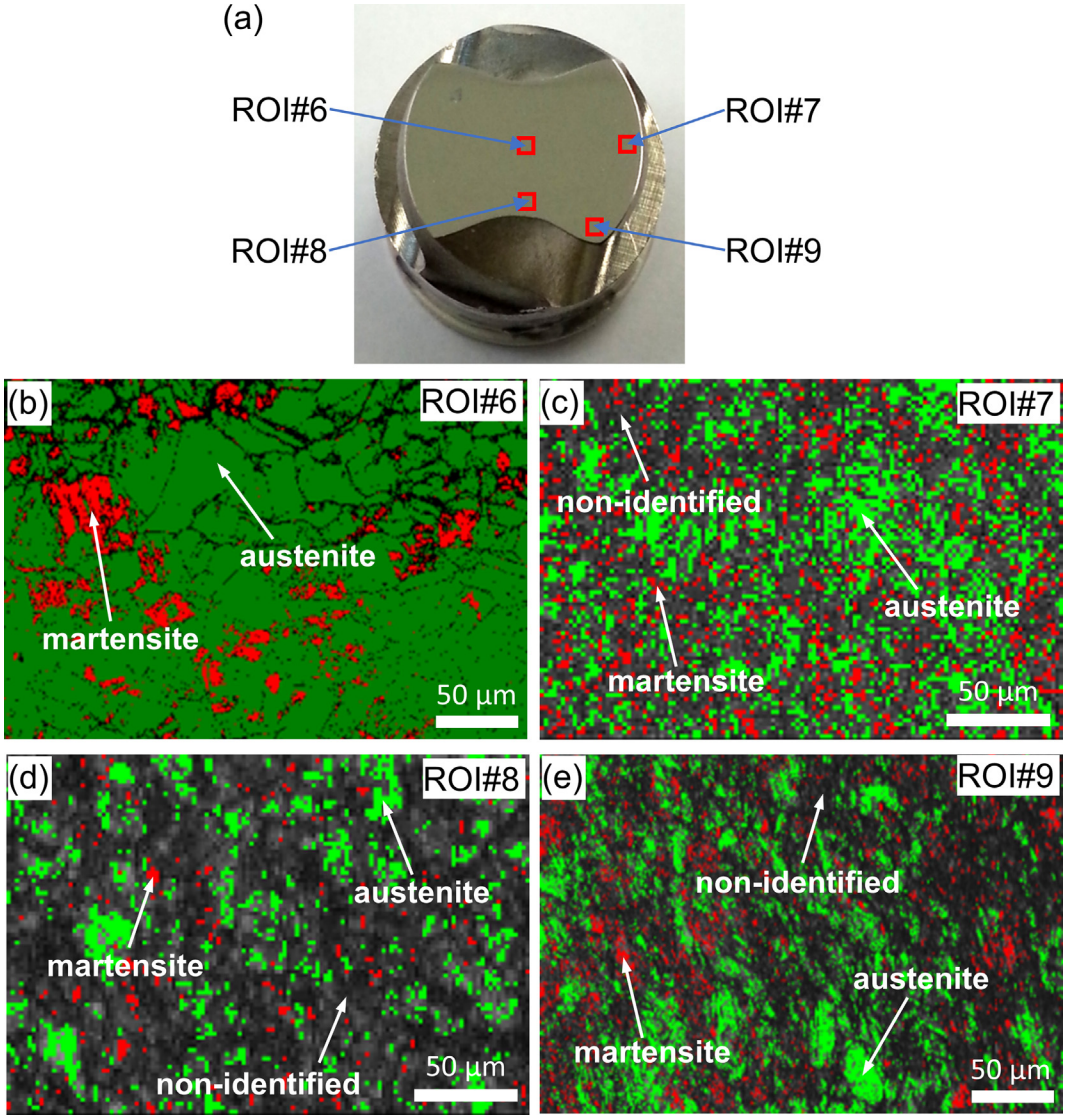

Fig. 8. Phase maps obtained by EBSD for selected regions of the sample twisted to 232°. (a) Photo of sample cut in the middle and positions at which EBSD maps were taken. (b–e) Phase maps where austenite (A) is green, martensite (M) is red, non-identified regions (Z) are black. (b) ROI#6 at the center of the sample (area fractions of A 77 %, M 8 %, Z 15 %). (c) ROI#7 at the middle of the short side of the sample (A 15 %, M 5 %, Z 80 %). (d) ROI#8 at the middle of the long side of the sample (A 22 %, M 9 %, Z 69 %). (e) ROI#9 at the corner of the sample (A 12 %, M 2 %, Z 86 %). (For interpretation of the references to color in this figure legend, the reader is referred to the web version of this article.)

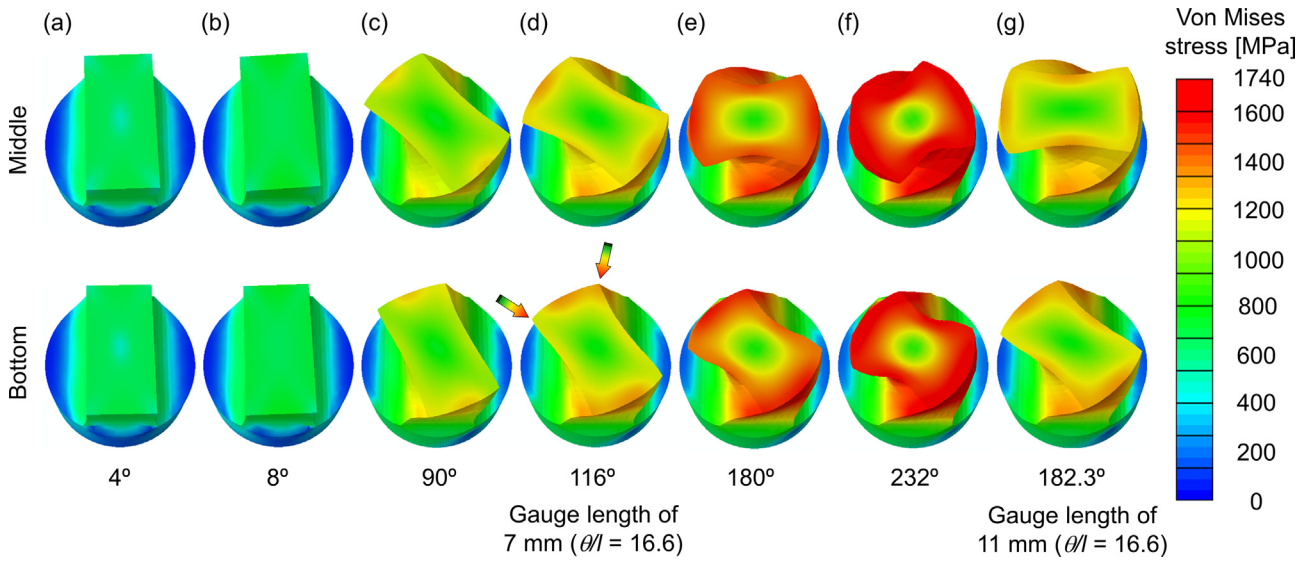

Fig. 9. Von Mises stress obtained by FEM for different twist angles of the steel specimen with a length of the employed gauge length of 7 mm. Twist angles of (a) 4°, (b) 8°, (c) 90°, (d) 116°, (e) 180°, (f) 232°. (g) A gauge length of 11 mm is included for comparison with the same ratio of twist/gauge length of 16.6 in (d).

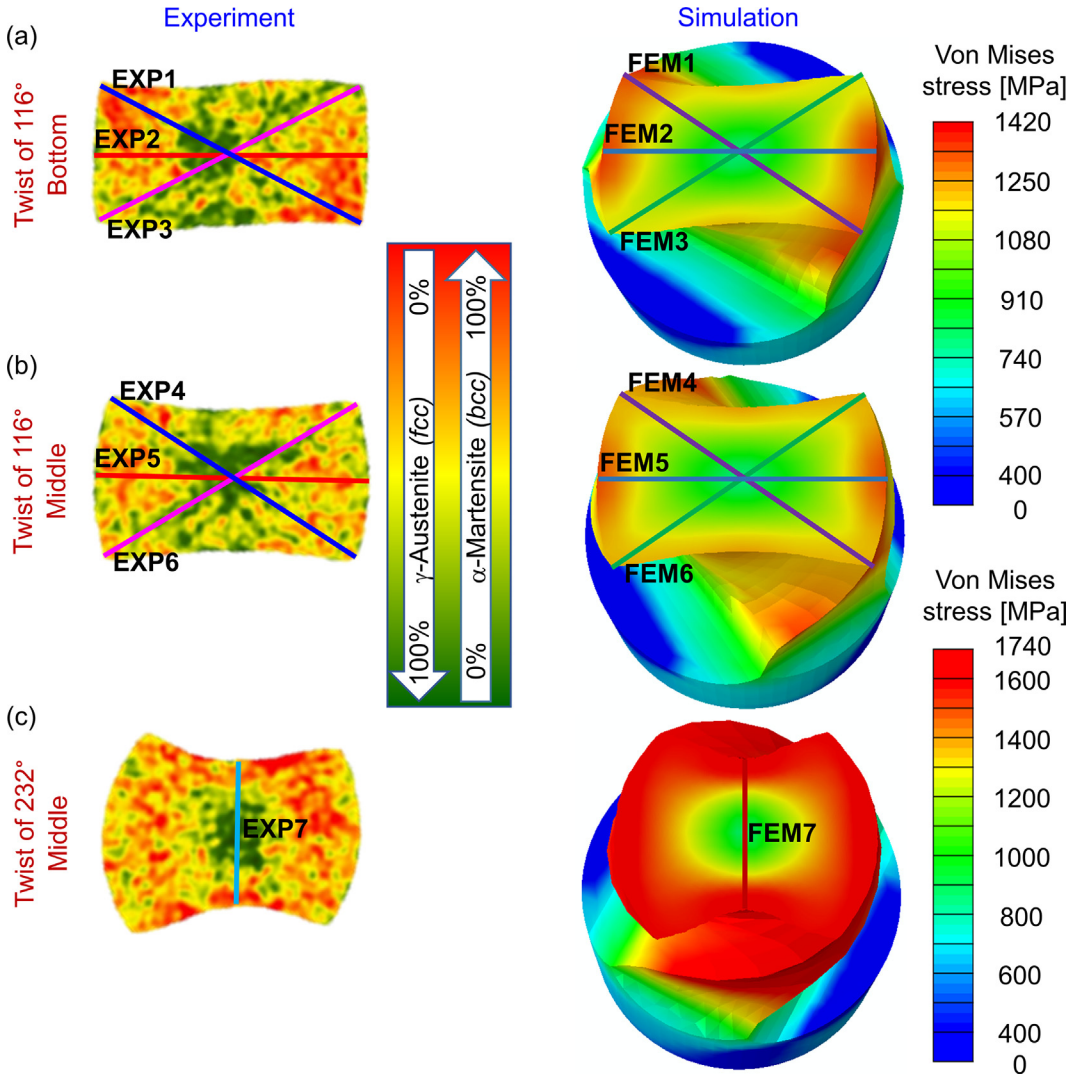

Fig. 10. Definition of the lines along which the profiles in Fig. 11 were determined, different twists and positions. (a) Twist of 116° at the bottom position. (b) Twist of 116° at the middle position. (c) Twist of 232° at the middle position.

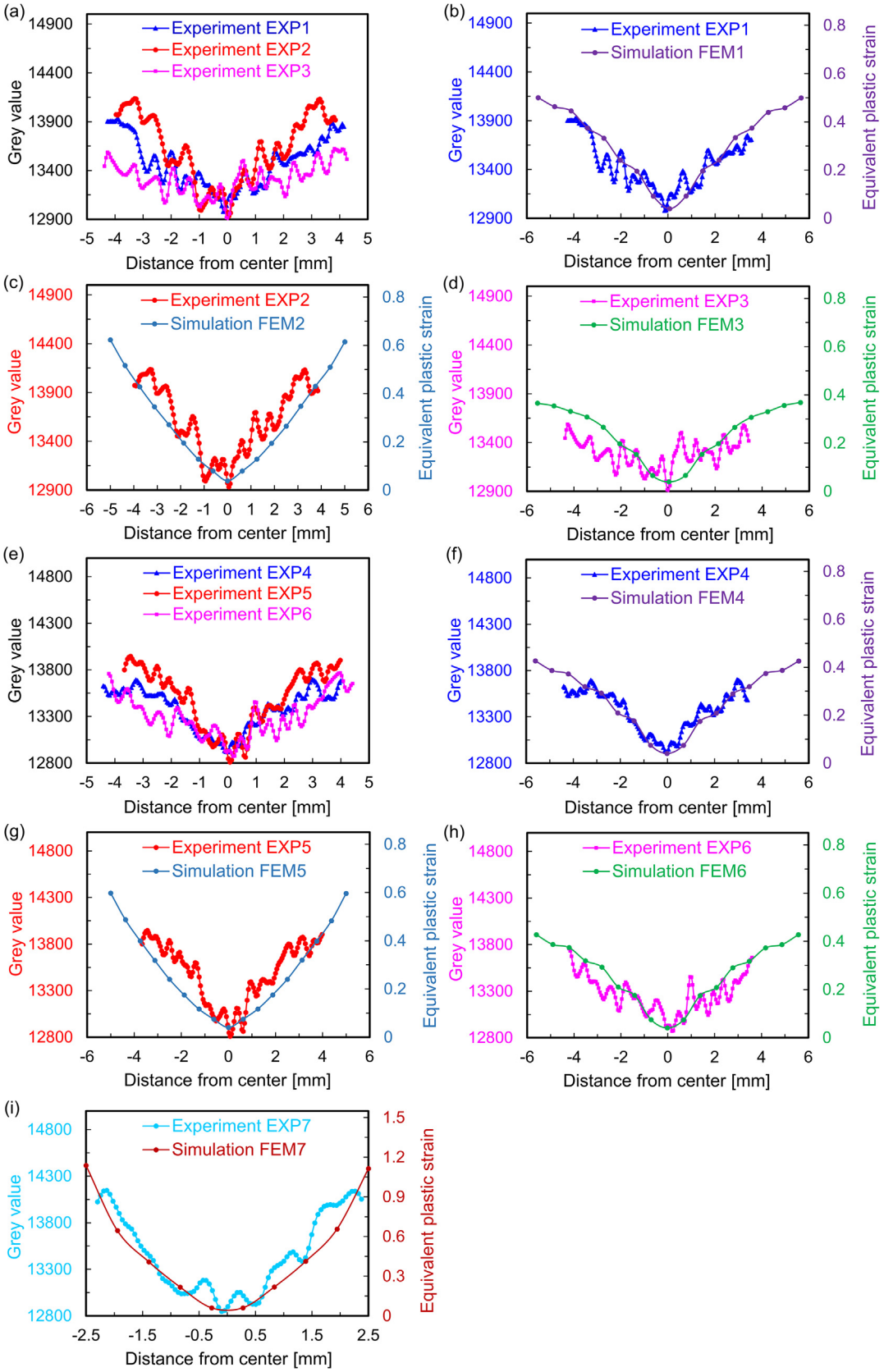

Fig. 11. Line profiles in various directions as defined in Fig. 10. Reconstructed tomographic data and FEM simulations are compared. (a–h) Twist angle 116 °C, (i) 232°. (a) Grey values at the bottom position of the sample for the different lines in Fig. 10a, namely EXP1, EXP2, and EXP3. (b) Grey value and shear strain for the lines of EXP1 and FEM1. (c) EXP2, FEM2. (d) EXP3, FEM3. (e) Grey values at the middle position of the specimen for the different lines in Fig. 10b, namely EXP4, EXP5, and EXP6. (f) Grey value and shear strain for the lines of EXP4 and FEM4. (g) EXP5, FEM5. (h) EXP6, FEM6. (i) Grey value and shear strain at the middle position for the line in Fig. 10c, namely EXP7, FEM7 with the twist of 232°.

at the center of the cross-section and – generally speaking – increases towards the outer side of the sample. Looking at a small twist of 4°, the von Mises stresses at the corners of the rectangular cross-section are zero, which is consistent with the theory of elasticity as discussed before [52]. The results also indicate that the von Mises stresses are largest at the center of each of the four edges of the middle section with values higher on the short sides, while, in an idealized case, they are expected to be larger in the middle of the long side. Here, additional geometrical constraints due to the gauge length play a role. While the neutron tomography results appeared surprising at first, with an expectation of the largest amount of phase transformation to be observed in the middle of the long side, the FEM results support the experimental findings. As already mentioned, the gauge length was designed with l = 7 mm. To study the effect of the gauge length, we also modeled gauge lengths of l = 10, 11, 12, 14, and 15 mm (see Fig. 9 and Fig. S4 in the SI). The idealized von Mises stress distribution during elastic deformation only occurs in the middle of the gauge length if it is longer than 14 mm. Any shorter gauge lengths and regions towards the top and bottom of the gauge length are prone to geometrical boundary effects.

The sample with the gauge length of 7 mm (utilized in the experiment) exhibits a centrosymmetric von Mises stress distribution in the middle of the gauge length throughout all deformation stages. However, the von Mises stresses on the long side are much less than those on the short side unlike in samples with longer gauge lengths. When the sample is twisted beyond 8°, the sample starts to experience large plastic deformations in some regions, also causing the corner of the sample to experience significant stress. Even more striking is the difference towards the top and bottom of the 7 mm gauge length. Here, it can be seen that two opposing corners experience the highest stress, while the other two corners experience significantly lower stress magnitudes (indicated by the arrows on Fig. 9). This clearly agrees with the experimental observations by neutron tomography (as well as optical microscopy and EBSD).

In order to compare and visualize the FEM results together with the phase distributions obtained by neutron tomography, line profiles as defined in Fig. 10 are drawn in Fig. 11, which shows the equivalent plastic strain magnitudes and grey values from the tomographic data distributions across the width, length and diagonal of the samples and the corresponding FEM results, which are in good agreement with each other. Measurements and simulations capture the symmetry effects well, including the effect of 'opposing corners' seen in Fig. 10a.

To further illustrate the similarities between the measured and simulated data, especially when investigating the cross-section away from the center of the gauge length, Fig. 12 depicts the asymmetric stress distributions in the corners at locations towards the top and bottom of the gauge length. One observes a close agreement between the spatial distributions of simulated stress and measured martensitic phase fractions. Moreover, the center of the long side in the middle section does not show a pronounced amount of martensite (which could be expected when considering the stress distribution in idealized rectangular members under elastic load) and again agrees with the stress distribution obtained by FEM. Only a longer gauge section may alter these results, as is included in Fig. 12c.

4. Conclusions

Alloys used in engineering components for structural applications will, in most cases, experience multiaxial mechanical stress states. However, the vast majority of studies that utilize deformation to address the microstructure-property relationships are based on uni-axial loading. When applying more complex deformation modes (e.g., bending, biaxial loading, torsion), one complexity for a representative microstructure investigation is related to localized phenomena and inhomogeneous microstructure distributions. Diffraction contrast in neutron imaging provides a powerful contrast mechanism to reveal such inhomogeneities as several examples in literature have shown, however, data interpretation has to be carried out with great care as the transmission signal is highly convoluted. A major contribution to the signal is the directional dependency of the grain alignment so that Bragg's law can be fulfilled and neutrons are removed from the incident beam by diffraction. Whenever phase distributions are to be studied, one has to ensure that the observed contrast can be attributed

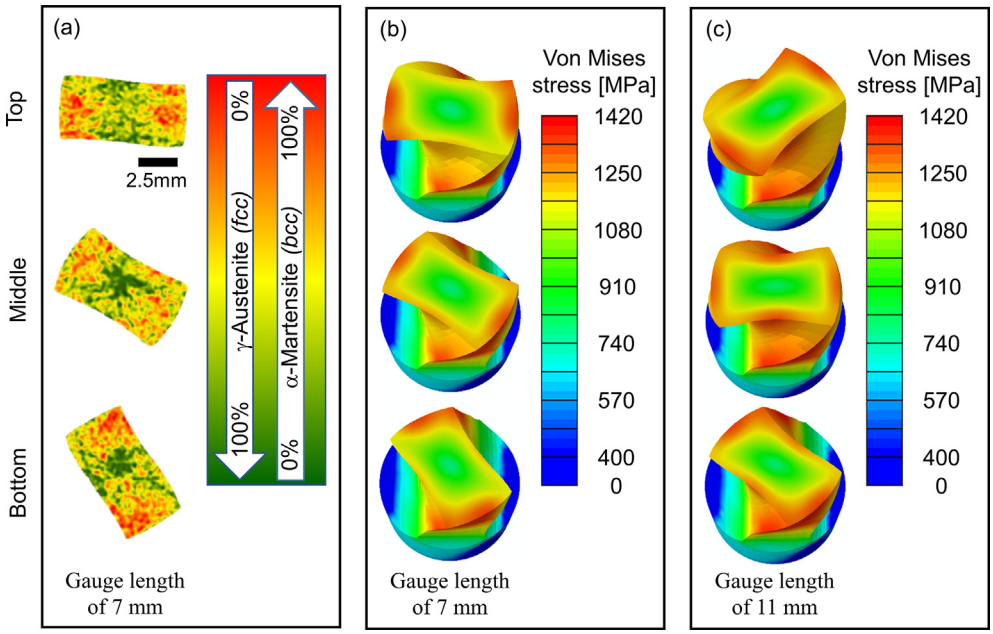

Fig. 12. Comparison of simulations based on two different gauge lengths and neutron tomography data at a ratio of twist/gauge length of 16.6°/mm. (a) Neutron tomography at a gauge length of 7 mm, (b) simulation at one of 7 mm, and (c) 11 mm.

to differences of crystallographic phase and are not a function of the sample orientation. In other words, only if the observed contrast variations are consistent for different sample orientations, do results from one single projection allow drawing conclusions about the phase distribution. Our results showcase a successful 3D tomographic reconstruction of irregular phase distribution in a sample of complex geometry and we employed additional characterization and simulation methods (OM, EBSD, FEM) to verify these results. Future methodologies and instrumentation should hence foresee to include deconvolution of transmission spectra of textured samples and/or to capture the diffracted beam simultaneously. The method has its key strength in the possibility to investigate bulk (cm-sized) parts non-destructively and in that it also works for heavily deformed materials. Potentially interesting applications could hence also include materials under severe plastic deformation (SPD) [58,60–63], where martensitic phase transformations are of interest.

We employed samples with a rectangular cross-section of 10 mm × 5 mm and subjected them to plastic deformation by torsion. Geometric boundary conditions influence the strain and stress distribution throughout deformation and result in a locally varying microstructure. Finite element modeling (FEM) was utilized with a focus on revealing stress distributions and allow for comparisons to the experimentally determined phase distributions. Implementation of more complex material point models would be desirable as they could yield an even more realistic prediction of phase transformation. In this case, microscale constitutive models could be linked to macroscopic boundary value problems through a (mesoscale) homogenization scheme with the advantage that critical microscale information can be properly taken into account in the macroscopic simulation and analysis similar to the work presented by Tjahjanto et al. [59].

CRediT authorship contribution statement

Khanh Van Tran: Methodology, Software, Investigation, Formal analysis, Writing – original draft, Visualization. **Robin Woracek:** Conceptualization, Methodology, Investigation, Formal analysis, Writing – original draft, Writing – review & editing, Visualization, Resources, Supervision. **Nikolay Kardjilov:** Conceptualization, Methodology, Software, Investigation, Formal analysis, Writing – original draft, Writing – review & editing, Visualization, Resources, Supervision. **Henning Markötter:** Software, Investigation, Writing – review & editing, Visualization. **Daniel Abou-Ras:** Investigation, Writing – review & editing. **Stephen Puplampu:** Investigation. **Christiane Förster:** Investigation. **Dayakar Penumadu:** Funding acquisition, Resources, Supervision. **Carl F.O. Dahlberg:** Software, Investigation, Writing – review & editing, Visualization. **John Banhart:** Resources, Writing – review & editing, Supervision. **Ingo Manke:** Funding acquisition, Resources, Writing – review & editing, Supervision, Methodology, Formal analysis.

Data availability

The raw data required to reproduce the findings of this study are available from the corresponding author on reasonable request.

Declaration of Competing Interest

The authors declare that they have no known competing financial interests or personal relationships that could have appeared to influence the work reported in this paper.

Acknowledgement

Funding: this work was supported by the Ministry of Education and Training of the Socialist Republic of Vietnam with project number 911 for overseas doctoral training.

Appendix A. Supplementary material

Supplementary data to this article can be found online at https://doi.org/10.1016/j.matdes.2022.111037.

References

[1] D. Raabe, B. Sun, A. Kwiatkowski Da Silva, B. Gault, H.-W. Yen, K. Sedighiani, P. Thoudden Sukumar, I.R. Souza Filho, S. Katnagallu, E. Jägle, P. Kürnsteiner, N. Kusampudi, L. Stephenson, M. Herbig, C.H. Liebscher, H. Springer, S. Zaefferer, V. Shah, S.-L. Wong, C. Baron, M. Diehl, F. Roters, D. Ponge, Current challenges and opportunities in microstructure-related properties of advanced high-strength steels, Metall. Mater. Trans. A 51 (11) (2020) 5517–5586, https://doi.org/10.1007/s11661-020-05947-2.
[2] M. Diehl, P. Shanthraj, P. Eisenlohr, F. Roters, Neighborhood influences on stress and strain partitioning in dual-phase microstructures: an investigation on synthetic polycrystals with a robust spectral-based numerical method, Mecc. - Comput. Micromech. Mater. 51 (2016) 429–441, https://doi.org/10.1007/s11012-015-0281-2.
[3] C.C. Tasan, M. Diehl, D. Yan, C. Zambaldi, P. Shanthraj, F. Roters, D. Raabe, Integrated experimental–simulation analysis of stress and strain partitioning in multiphase alloys, Acta Mater. 81 (2014) 386–400, https://doi.org/10.1016/j.actamat.2014.07.071.
[4] D. Brands, D. Balzani, L. Scheunemann, J. Schröder, H. Richter, D. Raabe, Computational modeling of dual-phase steels based on representative three-dimensional microstructures obtained from EBSD data, Arch. Appl. Mech. 86 (3) (2016) 575–598, https://doi.org/10.1007/s00419-015-1044-1.
[5] M. Kraska, M. Doig, D. Tikhomirov, D. Raabe, F. Roters, Virtual material testing for stamping simulations based on polycrystal plasticity, Comput. Mater. Sci. 46 (2009) 383–392, https://doi.org/10.1016/j.commatsci.2009.03.025.
[6] A. Ramazani, Z. Ebrahimi, U. Prahl, Study the effect of martensite banding on the failure initiation in dual-phase steel, Comput. Mater. Sci. 87 (2014) 241–247, https://doi.org/10.1016/j.commatsci.2014.01.051.
[7] F. Han, F. Roters, D. Raabe, Microstructure-based multiscale modeling of large strain plastic deformation by coupling a full-field crystal plasticity-spectral solver with an implicit finite element solver, Int. J. Plast. 125 (2020) 97–117, https://doi.org/10.1016/j.ijplas.2019.09.004.
[8] R.A. Lebensohn, A. Needleman, Numerical implementation of non-local polycrystal plasticity using fast Fourier transforms, J. Mech. Phys. Solids 97 (2016) 333–351, https://doi.org/10.1016/j.jmps.2016.03.023.
[9] P. Eisenlohr, M. Diehl, R.A. Lebensohn, F. Roters, A spectral method solution to crystal elasto-viscoplasticity at finite strains, Int. J. Plast. 46 (2013) 37–53, https://doi.org/10.1016/j.ijplas.2012.09.012.
[10] S. El Shawish, P.-G. Vincent, H. Moulinec, L. Cizelj, L. Gélébart, Full-field polycrystal plasticity simulations of neutron-irradiated austenitic stainless steel: a comparison between FE and FFT-based approaches, J. Nucl. Mater. 529 (2020) 151927, https://doi.org/10.1016/j.jnucmat.2019.151927.
[11] W. Reimers, A.R. Pyzalla, A. Schreyer, H. Clemens, Neutrons and Synchrotron Radiation in Engineering Materials Science. From Fundamentals to Material and Component Characterization, WILEY-VCH Verlag GmbH & Co. KGaA, Weinheim, 2008.
[12] M.T. Hutchings, P.J. Withers, T.M. Holden, T. Lorentzen, Introduction to the Characterization of Residual Stress by Neutron Diffraction, CRC Press, 2005.
[13] R. Woracek, J. Santisteban, A. Fedrigo, M. Strobl, Diffraction in neutron imaging—a review, Nucl. Instrum. Methods Phys. Res. Sect. A Accel. Spectrometers Detect. Assoc. Equip. 878 (2018) 141–158, https://doi.org/10.1016/j.nima.2017.07.040.
[14] N. Kardjilov, I. Manke, R. Woracek, A. Hilger, J. Banhart, Advances in neutron imaging, Mater. Today 21 (2018) 652–672, https://doi.org/10.1016/j.mattod.2018.03.001.
[15] M. Strobl, R. Harti, C. Gruenzweig, R. Woracek, J. Plomp, Small angle scattering in neutron imaging - a review, J. Imaging. 3 (4) (2017) 64, https://doi.org/10.3390/jimaging3040064.
[16] S.N. Monteiro, S. Paciornik, From historical backgrounds to recent advances in 3D characterization of materials: an overview, JOM 69 (2017) 84–92, https://doi.org/10.1007/s11837-016-2203-8.
[17] M.D. Uchic, L. Holzer, B.J. Inkson, E.L. Principe, P. Munroe, Three-dimensional microstructural characterization using focused ion beam tomography, MRS Bull. 32 (2007) 408–416, https://doi.org/10.1557/mrs2007.64.
[18] R. Woracek, D. Penumadu, N. Kardjilov, A. Hilger, M. Boin, J. Banhart, I. Manke, 3D mapping of crystallographic phase distribution using energy-selective neutron tomography, Adv. Mater. 26 (2014) 4069–4073, https://doi.org/10.1002/adma.201400192.
[19] R. Woracek, D. Penumadu, N. Kardjilov, A. Hilger, M. Boin, J. Banhart, I. Manke, Neutron Bragg edge tomography for phase mapping, Phys. Proc. (2015) 227–236, https://doi.org/10.1016/j.phpro.2015.07.032.

[20] C. Carminati, M. Strobl, T. Minniti, P. Boillat, J. Hovind, M. Morgano, T. Holm Rod, E. Polatidis, J. Valsecchi, D. Mannes, W. Kockelmann, A. Kaestner, Bragg-edge attenuation spectra at voxel level from 4D wavelength-resolved neutron tomography 4D wavelength-resolved neutron tomography, J. Appl. Crystallogr. 53 (2020) 188–196, https://doi.org/10.1107/S1600576720000151.
[21] A. Steuwer, J.R. Santisteban, P.J. Withers, L. Edwards, Pattern decomposition and quantitative-phase analysis in pulsed neutron transmission, Phys. B Condens. Matter. 350 (2004) 159–161, https://doi.org/10.1016/j.physb.2004.04.018.
[22] S. Vogel, A Rietveld-approach for the analysis of neutron time-of-flight transmission data, Christian-Albrechts Universität zu Kiel, PhD Thesis, 2000, Available from <https://macau.uni-kiel.de/receive/diss_mods_00000330>.
[23] K.V. Tran, R. Woracek, N. Kardjilov, H. Markötter, A. Hilger, W. Kockelmann, J. Kelleher, S.B. Puplampu, D. Penumadu, A.S. Tremsin, J. Banhart, I. Manke, Spectral neutron tomography, Mater. Today Adv. 9 (2021), https://doi.org/10.1016/j.mtadv.2021.100132 100132.
[24] J.N. Hendriks, A.W.T. Gregg, C.M. Wensrich, A.S. Tremsin, T. Shinohara, M. Meylan, E.H. Kisi, V. Luzin, O. Kirsten, Bragg-edge elastic strain tomography for in situ systems from energy-resolved neutron transmission imaging, Phys. Rev. Mater. 1 (5) (2017), https://doi.org/10.1103/PhysRevMaterials.1.053802 053802.
[25] W.R.B. Lionheart, Histogram tomography, ArXiv Prepr. ArXiv1809.10446, 2018, doi: 10.3934/mine.2020004.
[26] E. Cakmak, H. Choo, K. An, Y. Ren, A synchrotron X-ray diffraction study on the phase transformation kinetics and texture evolution of a TRIP steel subjected to torsional loading, Acta Mater. 60 (2012) 6703–6713, https://doi.org/10.1016/j.actamat.2012.08.040.
[27] J. Franců, P. Nováčková, P. Janíček, Torsion of a non-circular bar, Eng. Mech. 19 (2012) 45–60.
[28] L.M. Angelo Danao, R.M. Cabrera, Torsion of a rectangular prismatic bar: solution using a power fit model, Philipp. Eng. J. 28 (2007) 77–98.
[29] E. Polatidis, J. Čapek, A. Arabi-Hashemi, C. Leinenbach, M. Strobl, High ductility and transformation-induced-plasticity in metastable stainless steel processed by selective laser melting with low power, Scr. Mater. 176 (2020) 53–57, https://doi.org/10.1016/j.scriptamat.2019.09.035.
[30] F. Roters, M. Diehl, P. Shanthraj, P. Eisenlohr, C. Reuber, S.L. Wong, T. Maiti, A. Ebrahimi, T. Hochrainer, H.-O. Fabritius, S. Nikolov, M. Friák, N. Fujita, N. Grilli, K.G.F. Janssens, N. Jia, P.J.J. Kok, D. Ma, F. Meier, E. Werner, M. Stricker, D. Weygand, D. Raabe, DAMASK – The Düsseldorf Advanced Material Simulation Kit for modeling multi-physics crystal plasticity, thermal, and damage phenomena from the single crystal up to the component scale, Comput. Mater. Sci. 158 (2019) 420–478, https://doi.org/10.1016/j.commatsci.2018.04.030.
[31] ABAQUS Version 6.14, User's Manual. Inc Dassault Systemes Simulia, 2014, Available from <http://130.149.89.49:2080/v6.14/>.
[32] Multiphysics Object-Oriented Simulation Environment (MOOSE), n.d., Available from <https://mooseframework.inl.gov/>.
[33] M. Yaghoobi, S. Ganesan, S. Sundar, A. Lakshmanan, S. Rudraraju, J.E. Allison, V. Sundararaghavan, PRISMS-plasticity: an open-source crystal plasticity finite element software, Comput. Mater. Sci. 169 (2019), https://doi.org/10.1016/j.commatsci.2019.109078 109078.
[34] H.D.R. Sam Jordan, Hans-Joerg Frieden, Thomas Frieden, WARP3D, n.d., Available from <http://www.warp3d.net/>.
[35] V. Bedekar, R. Voothaluru, Q. Xie, A. Stoica, R.S. Hyde, K. An, In-situ neutron diffraction analysis of crystal plasticity of retained austenite in bearing steel, Proc. Eng. 207 (2017) 1958–1963, https://doi.org/10.1016/j.proeng.2017.10.968.
[36] V. Bedekar, R. Voothaluru, D. Yu, A. Wong, E. Galindo-Nava, S.B. Gorti, K.e. An, R.S. Hyde, Effect of nickel on the kinematic stability of retained austenite in carburized bearing steels - in-situ neutron diffraction and crystal plasticity modeling of uniaxial tension tests in AISI 8620, 4320 and 3310 steels, Int. J. Plast. 131 (2020) 102748, https://doi.org/10.1016/j.ijplas.2020.102748.
[37] Y. Gui, D. An, F. Han, X. Lu, G. Kang, X.u. Zhang, Multiple-mechanism and microstructure-based crystal plasticity modeling for cyclic shear deformation of TRIP steel, Int. J. Mech. Sci. 222 (2022) 107269, https://doi.org/10.1016/j.ijmecsci.2022.107269.
[38] P. Hou, Y. Li, W. Zhang, D. Chae, J.S. Park, Y. Ren, Y. Gao, H. Choo, Synchrotron x-ray diffraction and crystal plasticity modeling study of martensitic transformation, texture development, and stress partitioning in deep-drawn TRIP steels, Materialia 18 (2021), https://doi.org/10.1016/j.mtla.2021.101162 101162.
[39] M. Soleimani, A. Kalhor, H. Mirzadeh, Transformation-induced plasticity (TRIP) in advanced steels: a review, Mater. Sci. Eng., A 795 (2020), https://doi.org/10.1016/j.msea.2020.140023 140023.
[40] V.F. Zackay, E.R. Parker, D. Fahr, R. Busch, The enhancement of ductility in high-strength steels, ASM Trans Quart. 60 (1967) 252–259.
[41] M. Bayerlein, H.-J. Christ, H. Mughrabi, Plasticity-induced martensitic transformation during cyclic deformation of AISI 304L stainless steel, Mater. Sci. Eng., A 114 (1989) L11–L16, https://doi.org/10.1016/0921-5093(89)90871-X.
[42] R. Woracek, Energy selective neutron imaging for the characterization of polycrystalline materials, The University of Tennessee, Knoxville, PhD Thesis, 2015, Available from https://trace.tennessee.edu/utk_graddiss/3375.
[43] R. Woracek, D. Penumadu, N. Kardjilov, A. Hilger, M. Strobl, R.C. Wimpory, I. Manke, J. Banhart, Neutron Bragg-edge-imaging for strain mapping under in situ tensile loading, J. Appl. Phys. 109 (9) (2011) 093506, https://doi.org/10.1063/1.3582138.
[44] Correlated Solutions, n.d., Available from <https://www.correlatedsolutions.com/> (accessed June 7, 2020).
[45] J.R. Santisteban, L. Edwards, M.E. Fitzpatrick, A. Steuwer, P.J. Withers, M.R. Daymond, M.W. Johnson, N. Rhodes, E.M. Schooneveld, Strain imaging by Bragg edge neutron transmission, Nucl. Instrum. Methods Phys. Res. A. 481 (2002) 765–768, https://doi.org/10.1016/S0168-9002(01)01256-6.
[46] K. Iwase, K. Sakuma, T. Kamiyama, Y. Kiyanagi, Bragg-edge transmission imaging of strain and microstructure using a pulsed neutron source, Nucl. Instrum. Methods Phys. Res. Sect. A Accel. Spectrometers, Detect. Assoc. Equip. 605 (2009) 1–4, https://doi.org/10.1016/j.nima.2009.01.193.
[47] E.H. Lehmann, G. Frei, P. Vontobel, L. Josic, N. Kardjilov, A. Hilger, W. Kockelmann, A. Steuwer, The energy-selective option in neutron imaging, Nucl. Instrum. Methods Phys. Res. Sect. A Accel. Spectrometers, Detect. Assoc. Equip. 603 (2009) 429–438, https://doi.org/10.1016/j.nima.2009.02.034.
[48] W. Treimer, M. Strobl, N. Kardjilov, A. Hilger, I. Manke, Wavelength tunable device for neutron radiography and tomography, Appl. Phys. Lett. 89 (20) (2006) 203504, https://doi.org/10.1063/1.2384801.
[49] A.M. Al-Falahat, N. Kardjilov, T.V. Khanh, H. Markötter, M. Boin, R. Woracek, F. Salvemini, F. Grazzi, A. Hilger, S.S. Alrwashdeh, J. Banhart, I. Manke, Energy-selective neutron imaging by exploiting wavelength gradients of double crystal monochromators—simulations and experiments, Nucl. Instrum. Methods Phys. Res., Sect. A 943 (2019) 162477, https://doi.org/10.1016/j.nima.2019.162477.
[50] N. Kardjilov, A. Hilger, I. Manke, R. Woracek, J. Banhart, CONRAD-2: the new neutron imaging instrument at the Helmholtz-Zentrum Berlin, J. Appl. Crystallogr. 49 (2016) 195–202, https://doi.org/10.1107/S1600576715023353.
[51] K. Watanabe, T. Minniti, H. Sato, A.S. Tremsin, W. Kockelmann, R. Dalgliesh, Y. Kiyanagi, Cross-sectional imaging of quenched region in a steel rod using energy-resolved neutron tomography, Nucl. Instrum. Methods Phys. Res., Sect. A 944 (2019) 162532, https://doi.org/10.1016/j.nima.2019.162532.
[52] N.R. Blauld, Mechanics of Materials, Brooks/Cole Engineering Division, Monterey, CA, 1982.
[53] J. Li, C. Fang, Y. Liu, Z. Huang, S. Wang, Q. Mao, Y. Li, Deformation mechanisms of 304L stainless steel with heterogeneous lamella structure, Mater. Sci. Eng., A 742 (2019) 409–413, https://doi.org/10.1016/j.msea.2018.11.047.
[54] C. Maurice, R. Fortunier, A 3D Hough transform for indexing EBSD and Kossel patterns, J. Microsc. 230 (2008) 520–529, https://doi.org/10.1111/j.1365-2818.2008.02045.x.
[55] T. Karthikeyan, M.K. Dash, S. Saroja, M. Vijayalakshmi, Evaluation of misindexing of EBSD patterns in a ferritic steel, J. Microsc. 249 (2013) 26–35, https://doi.org/10.1111/j.1365-2818.2012.03676.x.
[56] A.J. Wilkinson, T.B. Britton, J. Jiang, P.S. Karamched, A review of advances and challenges in EBSD strain mapping, in: IOP Conf. Ser. Mater. Sci. Eng., Institute of Physics Publishing, 2014, doi: 10.1088/1757-899X/55/1/012020.
[57] C. Örnek, D.L. Engelberg, Correlative EBSD and SKPFM characterisation of microstructure development to assist determination of corrosion propensity in grade 2205 duplex stainless steel, J. Mater. Sci. 51 (2016) 1931–1948, https://doi.org/10.1007/s10853-015-9501-3.
[58] A. Azushima, R. Kopp, A. Korhonen, D.Y. Yang, F. Micari, G.D. Lahoti, P. Groche, J. Yanagimoto, N. Tsuji, A. Rosochowski, A. Yanagida, Severe plastic deformation (SPD) processes for metals, CIRP Ann. - Manuf. Technol. 57 (2008) 716–735, https://doi.org/10.1016/j.cirp.2008.09.005.
[59] D.D. Tjahjanto, P. Eisenlohr, F. Roters, Multiscale deep drawing analysis of dual-phase steels using grain cluster-based RGC scheme, Model. Simul. Mater. Sci. Eng. 23 (4) (2015) 045005, https://doi.org/10.1088/0965-0393/23/4/045005.
[60] C. Wang, F. Li, B. Chen, Z. Yuan, H. Lu, Severe plastic deformation techniques for bulk ultra-fine-grained materials, Xiyou Jinshu Cailiao Yu Gongcheng/Rare Met Mater. Eng. 41 (2012) 941–946, https://doi.org/10.1016/s1875-5372(12)60049-6.
[61] R.N. Harsha, V. Mithun Kulkarni, B. Satish Babu, Severe plastic deformation - a review, Mater. Today:. Proc. 5 (10) (2018) 22340–22349, https://doi.org/10.1016/j.matpr.2018.06.600.
[62] V. Segal, Review: modes and processes of severe plastic deformation (SPD), Materials (Basel) 11 (7) (2018) 1175, https://doi.org/10.3390/ma11071175.
[63] S. Swaminathan, M. Ravi Shankar, B.C. Rao, W.D. Compton, S. Chandrasekar, A. H. King, K.P. Trumble, Severe plastic deformation (SPD) and nanostructured materials by machining, J. Mater. Sci. 42 (2007) 1529–1541, https://doi.org/10.1007/s10853-006-0745-9.